Article

Wind–Wave Coupling Effect on the Dynamic Response of a Combined Wind–Wave Energy Converter

Jinghui Li [1], Wei Shi [1,*], Lixian Zhang [1], Constantine Michailides [2] and Xin Li [3]

1. State Key Laboratory of Coastal and Offshore Engineering, Deepwater Engineering Research Center, Dalian University of Technology, Dalian 116024, China; jinghuili@mail.dlut.edu.cn (J.L.); 2248742388@mail.dlut.edu.cn (L.Z.)
2. Department of Civil Engineering and Geomatics, Cyprus University of Technology, Limassol 3036, Cyprus; c.michailides@cut.ac.cy
3. Institute of Earthquake Engineering, Faculty of Infrastructure Engineering, Dalian University of Technology, Dalian 116024, China; lixin@dlut.edu.cn
* Correspondence: weishi@dlut.edu.cn; Tel.: +86-411-8470-8709

Abstract: There is a huge energy demand from offshore renewable energy resources. To maximize the use of various renewable energy sources, a combined floating energy system consisting of different types of energy devices is an ideal option to reduce the levelized cost of energy (LCOE) by sharing the infrastructure of the platform and enhancing the power production capacity. This study proposed a combined concept of energy systems by combing a heave-type wave energy converter (WEC) with a semisubmersible floating wind turbine. In order to investigate the power performance and dynamic response of the combined concept, coupled aero-hydro-servo-elastic analysis was carried out using the open-source code F2A, which is based on the coupling of the FAST and AQWA tools by integrating all the possible environmental loadings (e.g., aerodynamic, hydrodynamic). Numerical results obtained by AQWA are used to verify the accuracy of the coupled model in F2A in predicting dynamic responses of the combined system. The main hydrodynamic characteristics of the combined system under typical operational conditions were examined, and the calculated responses (motions, mooring line tension and produced wave power) are discussed. Additionally, the effect of aerodynamic damping on the dynamic response of the combined system was examined and presented. Moreover, a second fully coupled analysis model was developed, and its response predictions were compared with the predictions of the model developed with F2A in order for the differences of the calculated responses resulted by the different modeling techniques to be discussed and explained. Finally, the survivability of the combined concept has been examined for different possible proposed survival modes.

Keywords: wind–wave energy structures; wind turbine; fully coupled analysis; hydrodynamic response; aerodynamic damping; wave energy converters

1. Introduction

In recent years, the field of offshore wind power generation has developed rapidly and has become the fastest-growing energy source for marine renewable energy. As of the end of 2020, the global wind power capacity reached 744 GW, with 50% increase over 2019 [1]. With the rapid development of offshore wind technology, offshore wind turbines are increasing in scale and size, and the scale of wind farms is also increasing. The national renewable energy laboratory (NREL) 5-MW reference wind turbine [2] and DTU 10-MW reference wind turbine [3] have been widely used in comparative studies. The largest offshore wind turbine MySE 16.0-242 16 MW with rotor diameter of 242 m was launched by Ming Yang Smart Energy in August of 2021. To further exploit the offshore wind from deep water, various floating offshore wind concepts were proposed including mainly spar, semisubmersible, tension leg platform (TLP), and barge. Compared to TLP and spar, the

semisubmersible platform is more feasible in various water depths and has low installation costs of the mooring system. At present, the concepts of semisubmersible wind turbines mainly include WindFloat [4], Dutch Tri-floater [5], Windsea [6], Windflo [7], braceless [8], V-shaped [9], OC4-DeepCwind [10], and so on. Wave energy is also a large energy source, with a much higher power density than wind power, but this energy technology is not fully commercialized at present due to its high cost and reliability issue. WECs can generally be categorized as oscillating bodies, oscillating water columns, and overtopping devices [11].

By sharing space, supporting structures, cables, and other infrastructure, combining floating wind turbine system and WEC can not only reduce the cost of the device but also capture wind and wave energy and greatly improve the utilization of renewable energy of the ocean. At present, many studies on numerical simulations and model tests based on different floating offshore wind concepts (barge, TLP, spar, and semisubmersible) combined with WEC have been carried out. Aboutalebi et al. [12,13] proposed to install an oscillating water column WEC on the barge platform to reduce the fatigue movement of the platform. In Michailides et al. [14], the required wind–wave analysis for harsh environmental conditions has been examined. Ren et al. [15] carried out an experimental and numerical study of dynamic response of a new combined TLP wind turbine and wave energy converter. Bachynski et al. [16] proposed a TLP combined three-point absorber WECs system and studied the performance under operational and extreme sea cases. Russo et al. [17], Tomasicchio et al. [18], and Xu et al. [19] carried out experimental studies of the dynamic characteristics of Spar Buoy Wind Turbine and studied its dynamic behavior. Hu et al. [20] carried out the optimal design of WEC and dynamic characteristics analysis of a hybrid system combing a semisubmersible floating wind platform (WindFloat) and WECs. Sarmiento et al. [21] carried out a new floating semisubmersible structure combined with WECs (three oscillating water columns, OWC) in order to characterize the performance of the platform and OWCs. The MARINA Platform project funded by the European Union [22] proposed a combined system of semisubmersible platforms with point absorption and oscillating water column WEC. Peiffer et al. [23] and Aubault et al. [24] carried out coupled dynamic analysis through numerical models and experimental models. Muliawan et al. [25,26] proposed a comprehensive concept that combines a spar-type floating wind turbine with a torus WEC (named STC). Wan et al. [27–29] studied the dynamic response of an STC under typical operational conditions and extreme conditions based on numerical and experimental methods. Another concept that combines a floating semisubmersible wind turbine and a flap-type WEC (named SFC) was proposed. Michailides et al. [30–32] systematically studied the integrated operation of SFCs through numerical and experimental models. Ren et al. [33] carried out experimental and numerical studies on the hydrodynamic response of a new combined monopile wind turbine and a heaving-type WEC under typical operational conditions. In addition, Wang et al. [34] studied the hydrodynamic response of the combined system of the semisubmersible platform and heaving-type WEC.

With the development of the field of offshore wind turbines, the aero-hydro-servo-elastic coupling tool has become the key to solve the equation of motion and calculate the dynamic response of floating wind turbines. Different simulation tools have been developed so far. DeepLines [35,36], DARwind [37], Bladed, HAWC2, and FAST are the most well-known tools for fully coupled analysis of wind turbines. Jonkman et al. [38,39] developed a hydrodynamic module to consider the diffraction and radiation effects of floating platforms. Due to its open-source nature, it has also been used to participate in the development of a fully coupled framework. Kvittem et al. [40] combined AeroDyn with the non-linear finite element software SIMO/REFLEX. Shim [41] developed an interface that combines FAST with the fluid dynamic analysis tool CHARM3D. Recently, Yang et al. [42] developed a new aero-hydro-servo-elastic coupling framework based on FAST and AQWA (F2A) for dynamic analysis of FOWTs, combining the advantages of aero-elastic-servo of FAST and hydrodynamic analysis of AQWA [43].

In this study, with use of the recently proposed coupled analysis tool F2A, a fully coupled analysis is performed for a combined system consisting of a semisubmersible

platform and a heaving-type WEC. A numerical model of the combined structure that was capable of simulating its motion and dynamic responses under different typical operational conditions was developed and used with F2A. A second model with use of a different analysis tool is developed for performing fully coupled analysis. Different types of analysis and comparison were performed to examine the fully coupled responses of the combined structure but also for emphasizing the effect of different modeling methods/techniques on the response quantities of the combined system. The time-domain dynamic response characteristics, mooring characteristics, and PTO-produced power of the combined system are examined and presented in this study. Under the excitation of only waves, there was small difference between the two numerical models, while under irregular wave and turbulent wind conditions, the difference between two models was larger. The impact of aerodynamic loads as well as aerodynamic damping is significant. When the wind velocity is small, aerodynamic damping has a significant effect on reducing the resonance of surge and pitch, and there is an obvious positive relationship. When the wind velocity increases, wind thrust has a greater impact than aerodynamic damping. The rationality behind the efficient use of the two examined numerical tools for studying combined concepts has been presented. Finally, an extreme condition is studied to ensure the survivability of the combined system. The results show that the two models had significant differences in dynamic motion and mooring force prediction under irregular wave and turbulent wind condition due to the wind–wave coupling effect at low frequency range.

2. Theoretical Background

Different from offshore oil and gas platform, a floating wind turbine experiences the aerodynamic load and hydrodynamic load simultaneously. These loads are both important in the system design at the same order. The basic theories used in the combined system analysis are described in this section.

2.1. Aerodynamic Loads and Aerodynamic Damping

Blade element momentum (BEM) theory is one of the efficient and most commonly used methods for calculating induced loads on wind turbine blades [44]. In this theory, the wind turbine blade is divided into many sections along the span direction, and these sections are called blade elements. The wind turbine blade is simplified as a finite element that is superimposed in the radial direction, so the three-dimensional aerodynamic characteristics of the wind turbine blade can be obtained by integrating the aerodynamic characteristics of the element in the radial direction [42].

The axial velocity V_2 and the circumferential velocity V_3 at the rotor plane are calculated as follows:

$$V_2 = (1 - a)V_1 \tag{1}$$

$$V_3 = \Omega r (1 + a') \tag{2}$$

where V_1 is the incoming wind velocity, a is the axial induction factor, and a' is the angular induction factor. The axial velocity and the circumferential velocity vector are combined to obtain the resultant velocity V_0. The lift force (L) is formed perpendicular to the resultant velocity, and the drag force (D) is formed in the same direction as the incoming velocity. They can be calculated by the following equations:

$$L = \frac{1}{2}\rho V_0^2 A C_L \tag{3}$$

$$D = \frac{1}{2}\rho V_0^2 A C_D \tag{4}$$

where A is the rotor sweeping area, ρ is the air density, C_L is the lift coefficient, and C_D is the drag coefficient.

The lift coefficient C_L and drag coefficient C_D of the aerofoil are projected in the normal and tangential directions, respectively, to obtain the normal force coefficient C_N and the tangential force coefficient C_T, as shown in the following equations:

$$C_N = C_L \cos \varphi + C_D \sin \varphi \tag{5}$$

$$C_T = C_L \sin \varphi - C_D \cos \varphi \tag{6}$$

Finally, the thrust force and torque on the blade section are calculated by the following equations:

$$dT = \frac{1}{2}\rho V_0^2 c C_N dr \tag{7}$$

$$dM = \frac{1}{2}\rho V_0^2 c C_T r dr \tag{8}$$

where c is the aerofoil chord length.

When studying aerodynamic loads, the influence of aerodynamic damping cannot be ignored. Analyzed at the micro level, the aerodynamic damping of the wind turbine essentially comes from the relationship between the aerodynamic load of the wind turbine blades and the inflow wind velocity. Without considering the platform motion and elastic structure deformation [45], the following equation can be used:

$$V_0 = V_1 \sqrt{(1-a)^2 + \left[\frac{\Omega r}{V_0}(1+a')\right]^2} = V_1 f_1 \tag{9}$$

The factor f_1 indicates that the relative inflow wind velocity at the blade is simultaneously affected by the axial induction factor, angular induction factor, structural deformation of the wind turbine, and rotational velocity [46].

Considering the relative movement of the platform, the relative velocity is written as follows:

$$V_0 = V_1 f_1 - L\dot{x}_5 \cos(x_5) - \dot{x}_1 \tag{10}$$

where x_5 is the pitch motion of the platform, $\dot{x}_5$ is the pitch velocity of the platform, and $\dot{x}_1$ is the surge velocity of the platform.

From Equation (7), the total thrust T on the blade can be obtained as follows:

$$T \infty V_0^2 \infty \left(V_1 f_1 - L\dot{x}_5 \cos(\dot{x}_5) - \dot{x}_1\right)^2 \tag{11}$$

Ignoring the velocity components above the second order, the following equation is obtained:

$$\begin{aligned} T &\infty (V_1 f_1)^2 - 2V_1 f_1 L\dot{x}_5 \cos(\dot{x}_5) - 2V_1 f_1 \dot{x}_1 \\ &\infty (V_1 f_1)^2 - 2V_1 f_1 L\dot{x}_5 - 2V_1 f_1 \dot{x}_1 \end{aligned} \tag{12}$$

The last two terms in the above equation represent aerodynamic damping and can be added to the left side of the equation of motion. The aerodynamic thrust is proportional to the square of the wind velocity, and the aerodynamic damping is proportional to the first power of the wind velocity. This shows that when the wind velocity is not particularly high, the effect of aerodynamic damping on the offshore floating wind turbine may be more obvious, and the relationship between them is positive. However, as the wind velocity increases, the influence of aerodynamic thrust may be much greater than that of aerodynamic damping. Of course, the aerodynamic damping force of offshore floating wind turbines is affected not only by wind velocity but also by other complex factors, such as aerodynamic induction factor. Thrust coefficient may even be affected by pitch angle and stall effect. Since F2A and AQWA were used for simulation in this study, the largest difference between them is whether considering aerodynamic damping.

2.2. Potential Flow Theory

The potential flow theory may be to calculate the hydrodynamic loads on marine structures. It is usually assumed that the fluid is non-rotating, non-viscous, and incompressible, and the fluid is assumed to be an ideal fluid [47,48]. Derived from the conservation of mass and the conservation of momentum, the governing equations of fluid motion, the Laplace equation are expressed as follows:

$$\nabla^2 \phi = 0 \tag{13}$$

$$\frac{\partial u}{\partial t} + (u \cdot \nabla)u = -\nabla\left(gz + \frac{p}{\rho}\right) \tag{14}$$

where ϕ represents the three-dimensional velocity potential function and $\phi = \phi(x, y, z, t)$. The velocity potential can be decomposed into the following equation:

$$\phi = \phi^i + \phi^d + \phi^r \tag{15}$$

where ϕ^i is the velocity potential function of the incident wave, ϕ^d is the diffraction potential function, and ϕ^r is the radiation potential function.

For the fluctuation problem of linear periodic motion, the time factor can be separated by the variable separation method, and the velocity potential can be expressed as follows:

$$\phi = \text{Re}\left[\varphi e^{-i\omega t}\right] \tag{16}$$

where ω is the angular frequency and Re represents the real part.

2.3. Viscous Loads

In potential flow theory, since the assumption is inviscidity, viscosity needs to be considered in practice. In this study, the Morrison model was added to consider the viscosity [48,49]. In AQWA, the viscosity was simulated by adding Morrison elements as follows:

$$f_d = 0.5 C_d \rho D \mu |\mu| \tag{17}$$

where C_d represents the drag coefficient, and in this study, $C_d = 1.2$ was selected due to $d/L \geq 0.2$ and $H/d \leq 0.2$; H, d, and L represent the wave height, water depth, and wavelength, respectively; μ, D, and are the incoming flow velocity, structure diameter, and fluid density, respectively; and f_d represents the drag force on a unit height of the structure.

2.4. Equation of Motion

In this study, the wind and wave energy combined system consists of two bodies having in total 12 degrees of freedom (six degrees for each body), which requires comprehensive consideration of multiple degree-of-freedom systems [29]. The multi-body equation of motion is given as follows:

$$\begin{pmatrix} (M+m)_{11} & m_{12} \\ m_{21} & (M+m)_{22} \end{pmatrix}\begin{pmatrix} \ddot{x}_1(t) \\ \ddot{x}_2(t) \end{pmatrix} + \int_0^t \begin{pmatrix} \kappa(t-\tau)_{11} & \kappa(t-\tau)_{12} \\ \kappa(t-\tau)_{21} & \kappa(t-\tau)_{22} \end{pmatrix}\begin{bmatrix} \dot{x}_1(\tau) \\ \dot{x}_2(\tau) \end{bmatrix}d\tau$$
$$+ \begin{pmatrix} (R)_{11} & 0 \\ 0 & (R)_{22} \end{pmatrix}\begin{bmatrix} x_1(t) \\ x_2(t) \end{bmatrix} = \begin{bmatrix} f^{wind}(t) \\ 0 \end{bmatrix} + \begin{bmatrix} f_1{}^{wave}(t) \\ f_2{}^{wave}(t) \end{bmatrix} + \begin{bmatrix} f_1{}^{drag}(t) \\ f_2{}^{drag}(t) \end{bmatrix}$$
$$+ \begin{bmatrix} f_1{}^{interface}(t) \\ f_2{}^{interface}(t) \end{bmatrix} + \begin{bmatrix} F_1{}^{PTO}(t) \\ F_2{}^{PTO}(t) \end{bmatrix} \tag{18}$$

where m is the added mass matrix, x, $\dot{x}$, and $\ddot{x}$ are the displacement, velocity, and acceleration matrix in the time domain, respectively, $\kappa(\tau)$ is the retardation function, which is based on the added mass and potential damping matrix, and f is the summation of the external forces in time domain. The subscripts 1 and 11 refer to the variables of body 1 (braceless); subscripts 2 and 22 refer to the variables of body 2 (WEC); and subscripts 12 and 21 present the coupling terms between the braceless and WEC. The vertical (heave) quadratic damping of the braceless and WEC terms is modeled by the quadratic damping matrix on the left side of Equation (18). The term f^{wind} denotes wind load on the turbine rotor, while f^{wave} is the wave forces applied on the braceless platform and WEC. The

interface forces $f_1^{interface}$ between the two bodies include horizontal contact forces and vertical friction forces. F^{PTO} is the PTO forces. Each term of the interface and PTO forces is applied on the two bodies with the same value but in different directions.

2.5. Brief Description of F2A

The baseline version of AQWA was incapable of predicting the aero-servo-elastic of floating offshore wind turbines, but it accepted time domain analysis of external forces implemented by dynamic link library (.dll). In order to enable AQWA to form a fully coupled analysis of floating offshore wind turbines, FAST was integrated in AQWA with some simulation function implemented [36]. Therefore, the coupling framework was "FAST2AQWA", denoted as F2A. The coupling of AQWA and FAST was accomplished by user_force.dll and source code subroutine of FAST. Related simulation capabilities of FAST were completely implemented in time domain analysis in the DLL that can be called by AQWA during the simulation.

3. Numerical Model of Combined System

The combined system was composed of a semisubmersible platform and a heaving-type WEC connected by a guide-roller system in the middle and an upper connecting system [50]. The wind turbine model used for this study is the NREL 5-MW baseline wind turbine. The main parameters of the 5-MW wind turbine are shown in Table 1 [2]. An illustration of the combined system is shown in Figure 1, and the main parameters of the combined system are shown in Table 2. In this study, the time-domain hydrodynamic simulation of the combined system was based on AQWA. Hydrodynamic panel models are shown in Figure 2.

Table 1. The main parameters of the 5-MW wind turbine.

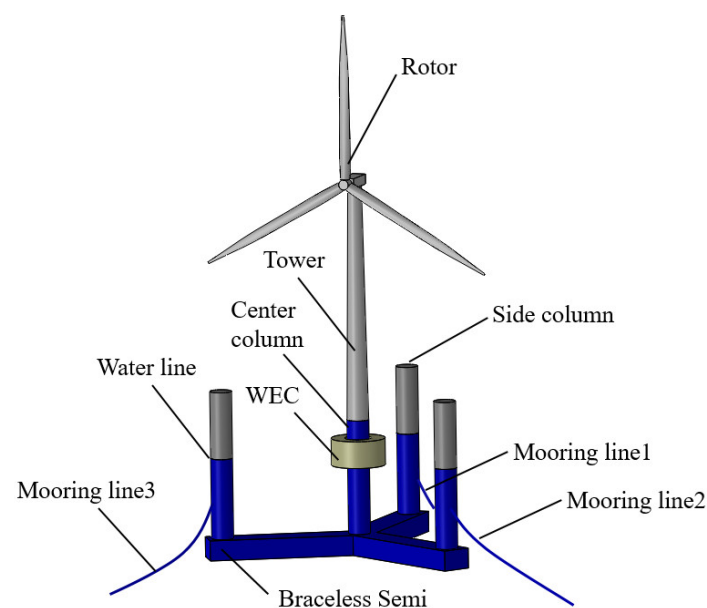| Rotor-Nacelle-Assembly t	350
Center of Gravity (CoG) m	$(-0.2, 0.0, 70)$
Tower mass t	347.46
Total WT mass moment of inertia about X axis (I_{xx}) kg*m^2	3,770,000,000
Total WT mass moment of inertia about Y axis (I_{yy}) kg*m^2	3,660,000,000
Total WT mass moment of inertia about Z axis (I_{zz}) kg*m^2	112,000,000

Figure 1. Sketch map of the combined system.

Table 2. The main parameters of the combined system.

	Parameters	Values
Semisubmersible platform	Semisubmersible mass t	9738
	Diameter of the central column m	6.5
	Diameter of the three side columns m	6.5
	Water displacement m^3	10,298
	Water depth m	200
	Operating draft m	30
	Center of semisubmersible m	(0,0,24.36)
WEC	Outer/Inner diameter m	16/8
	FigureHeight/Draft m	8/3.5
	Mass t	463.5
	Water displacement m^3	452.2
	Center of mass m	(0,0,1)
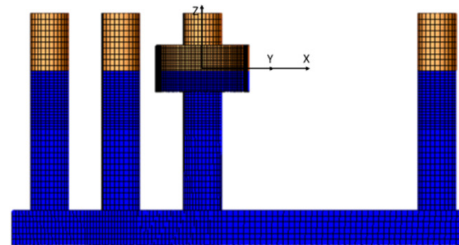
Figure 2. Panel models for the hydrodynamic analysis.

The PTO system (shown in Figure 3), which captures the wave energy through the relative heave motion of the semisubmersible platform and the WEC, was simplified as a linear spring and a linear damper. This model was accomplished by establishing a fender element in ANSYS/AQWA. Based on the discussion of damping coefficient of Fender and stiffness coefficient of linear spring [27–29,33,34,50], it was found that a large value of B_{pto} value may lead to air compressibility that cannot be ignored, while a small K_{pto} coefficient may ignore the influence of stiffness coefficient on the produced power [19]. Therefore, 1.5×10^6 Ns^2/m was selected for B_{pto} and 1 N/m for K_{pto} in this study. The force of PTO was calculated by the following equation:

$$F_{pto} = B_{pto} \cdot (v_2 - v_1) + K_{pto} \cdot (x_2 - x_1) \tag{19}$$

where B_{pto} and K_{pto} are the linear damping coefficient and linear spring stiffness coefficient, respectively; v_1 and x_1 are the velocity and displacement of the semisubmersible platform; and v_2 and x_2 are the velocity and displacement of the WEC, respectively.
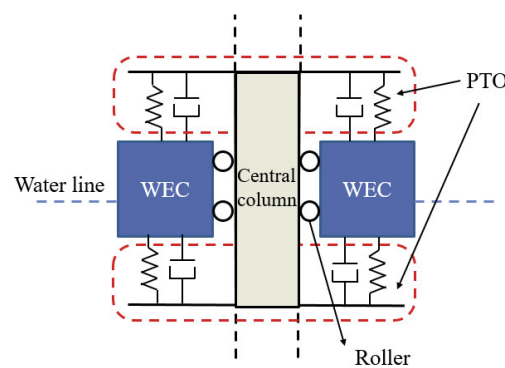

Figure 3. Simplified dynamic coupling model between the WEC and braceless.

Knowing the damping force of the PTO system and the relative velocity between the platform and WEC, the produced power of the WEC can be calculated through the following equation:

$$P_{PTO} = F_{PTO} \cdot (v_2 - v_1) \tag{20}$$

4. Results and Discussion

The simulations conducted in this study were primarily carried out under typical operational conditions and extreme conditions from a typical site at 61°21′ N latitude and 0°0′ E longitude near the Shetland Islands, northeast of Scotland, UK. The water depth at the site was 200 m [51]. The examined load cases are listed in Table 3. For regular wave case (LC1), the 1800 s–1900 s was used in the comparison to get rid of transient effect. For irregular wave cases (LC2–LC4), the total simulation time is 4600 s, and the first 1000 s has been excluded to avoid the transient effect. It should be noted that the time series results of the motion and force responses between 3500 to 3700 s are displayed to better present the difference between different codes.

Table 3. Load cases table.

Load Case	Wind Velocity U_{wind} (m/s)	Wave Height H/H_s (m)	Wave Period T/T_p (s)
LC1	/	2.0	9.0
LC2	8.4	2.0	14.8
LC3	11.4	2.4	10.9
LC4	23.8	5.5	13.5
LC5	50.0	13.8	19.2

4.1. Free Decay Test

A free decay test was performed in the numerical simulation to determine the natural frequencies of the surge, heave, and pitch of the platform. The natural frequencies are listed in Table 4. Figure 4 was the time domain curve of free decay test of platform. The results showed that the natural frequencies of the surge (Figure 4a) and heave (Figure 4b) of the platform were the same from two codes, and there is a difference of about 11.7% of the natural frequency of the platform pitch from two codes.

Table 4. Natural frequencies (rad/s) of platform.

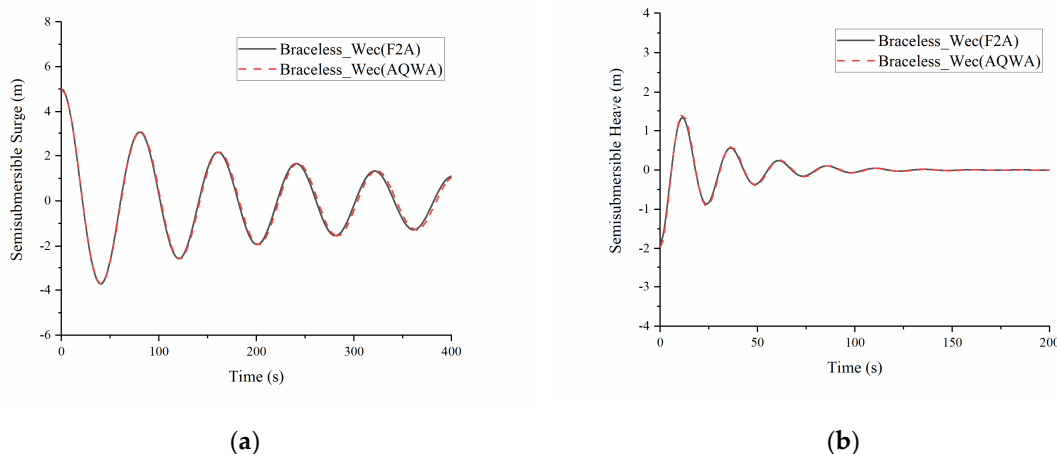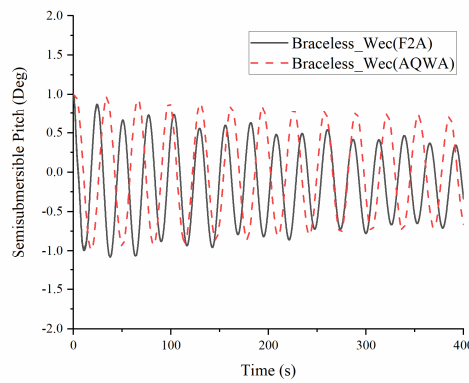|	Surge	Heave	Pitch
F2A	0.078	0.256	0.239
AQWA	0.078	0.256	0.210

(a)

(b)

Figure 4. *Cont.*

(**c**)

Figure 4. Time domain curve of free decay test of the semisubmersible platform: (**a**) Surge; (**b**) Heave; (**c**) Pitch.

4.2. Regular Wave Condition

In this study, the simulation of typical regular wave conditions (LC1) was performed, and the characteristics of the motion response, mooring response, and produced power of multiple bodies (F2A and AQWA simulation) were compared.
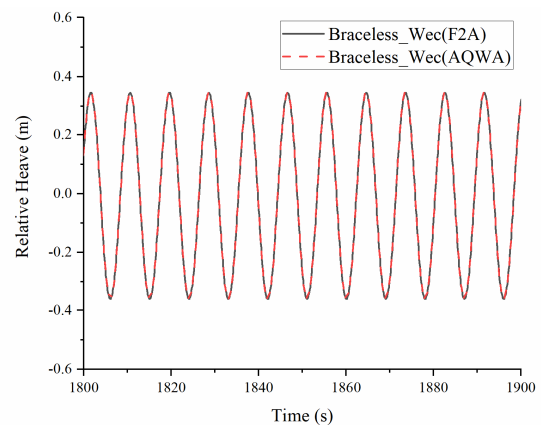
4.2.1. Motion Response

In this section, the motion response under a regular wave (H = 2.0 m, T = 9.0 s) was selected, and a motion response of three degrees of freedom (DOF) of the platform (surge, relative heave, pitch) is presented (Figure 5). The results were compared between the fully coupled framework F2A and the hydrodynamic software AQWA.

The surge motion of the platform is shown in Figure 5a. Compared with the multibody simulation results of F2A and AQWA, the amplitude was basically the same, but the simulation results of F2A at the wave peak were slightly larger. The relative heave motion responses simulated by F2A and AQWA were basically the same (Figure 5b). Slightly larger pitch response from F2A could be identified compared with AQWA results. Under only wave conditions, F2A and AQWA had good consistency in simulating multibody motion characteristics, especially in relative heave.
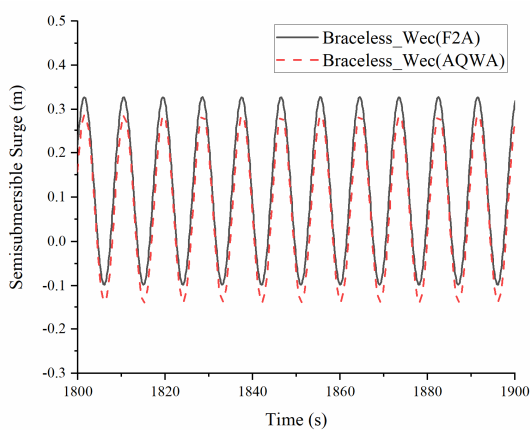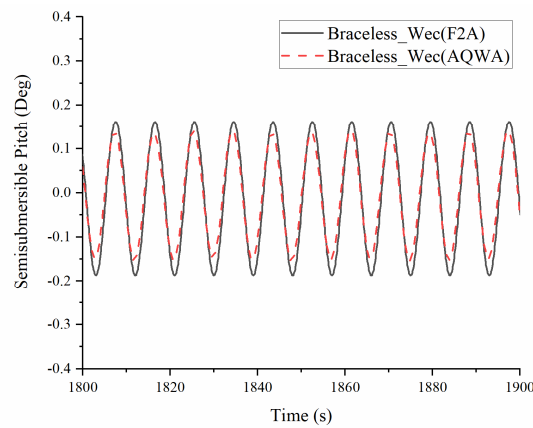

(**a**)

(**b**)

Figure 5. *Cont.*

(**c**)

Figure 5. Time domain motion response of the semisubmersible platform: (**a**) Surge; (**b**) Relative Heave; (**c**) Pitch.

4.2.2. Mooring Line Force

Figure 6 shows the time-domain response of the mooring force of Mooring Line 1 (ML1) and Mooring Line 2 (ML2). The mooring line force of ML1 (downwind direction) was smaller than that of ML2 (upwind direction) when subjected to waves in the heading direction. Results from F2A have slightly larger mooring line force than those from AQWA simulation.
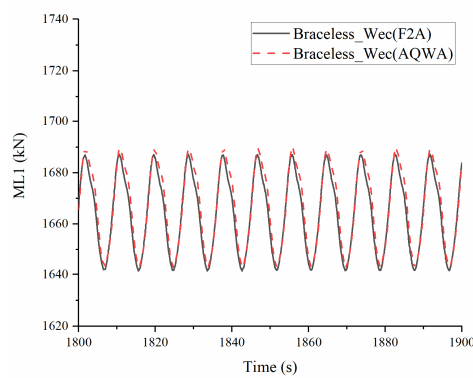
(**a**)
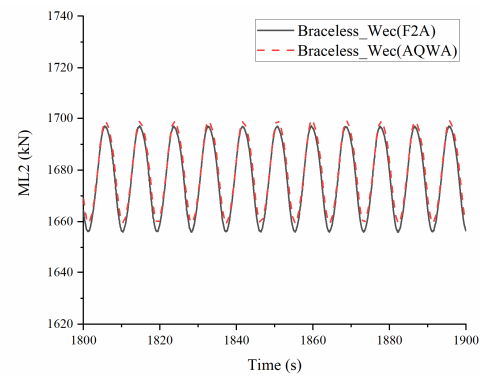
(**b**)

Figure 6. Mooring force of: (**a**) ML1; (**b**) ML2.

4.2.3. Produced Wave Power

The wave energy was captured by PTO system. The relative heave velocity from both codes are similar to each other (Figure 7a). From Equation (19), the damping force can be observed in Figure 7b. Based on the relative heave velocity and damping force, the produced wave power could be identified, which is similar from F2A results and AQWA results (Figure 7c).
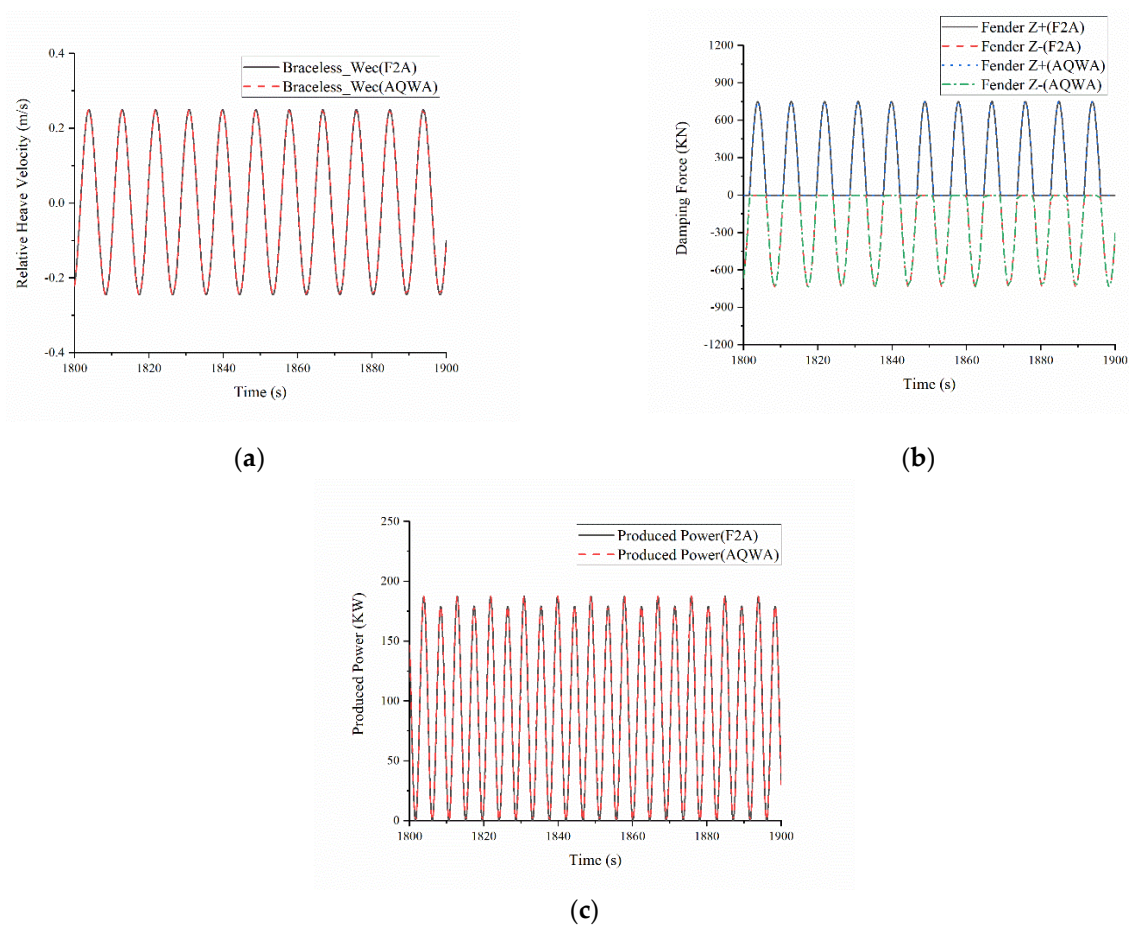
(a)

(b)

(c)

Figure 7. Time series of different responses of the combined structure under regular waves: (**a**) Relative Heave Velocity; (**b**) Damping Force; (**c**) Produced Power.

Under only wave conditions, F2A and AQWA had good consistency in simulations of the multibody dynamic response. This was because F2A integrates the AQWA hydrodynamic module.

4.3. Irregular Wave and Turbulent Wind Conditions

This section presents the motion response, mooring force, and produced power under irregular wave and turbulent wind conditions.

4.3.1. Motion Response

Figure 8 shows the motion response in surge, pitch, and heave directions under normal operation conditions in LC2 and LC3. The responses of surge and pitch in both load cases from F2A (Figure 8a,b) simulation are smaller than those predicted by AQWA (Figure 8e,f). This is due to the fact that the wind load in F2A and AQWA is differently implemented. In F2A, the wind field is pre-generated and both wind aerodynamic load and damping are considered due to the rotating turbine rotor. However, in AQWA, the wind load is implemented as an external load using dll function and no interaction and aerodynamic damping is included. The difference for the relative heave motions simulated by two tools was limited for both LC2 and LC3 (Figure 8c,d).
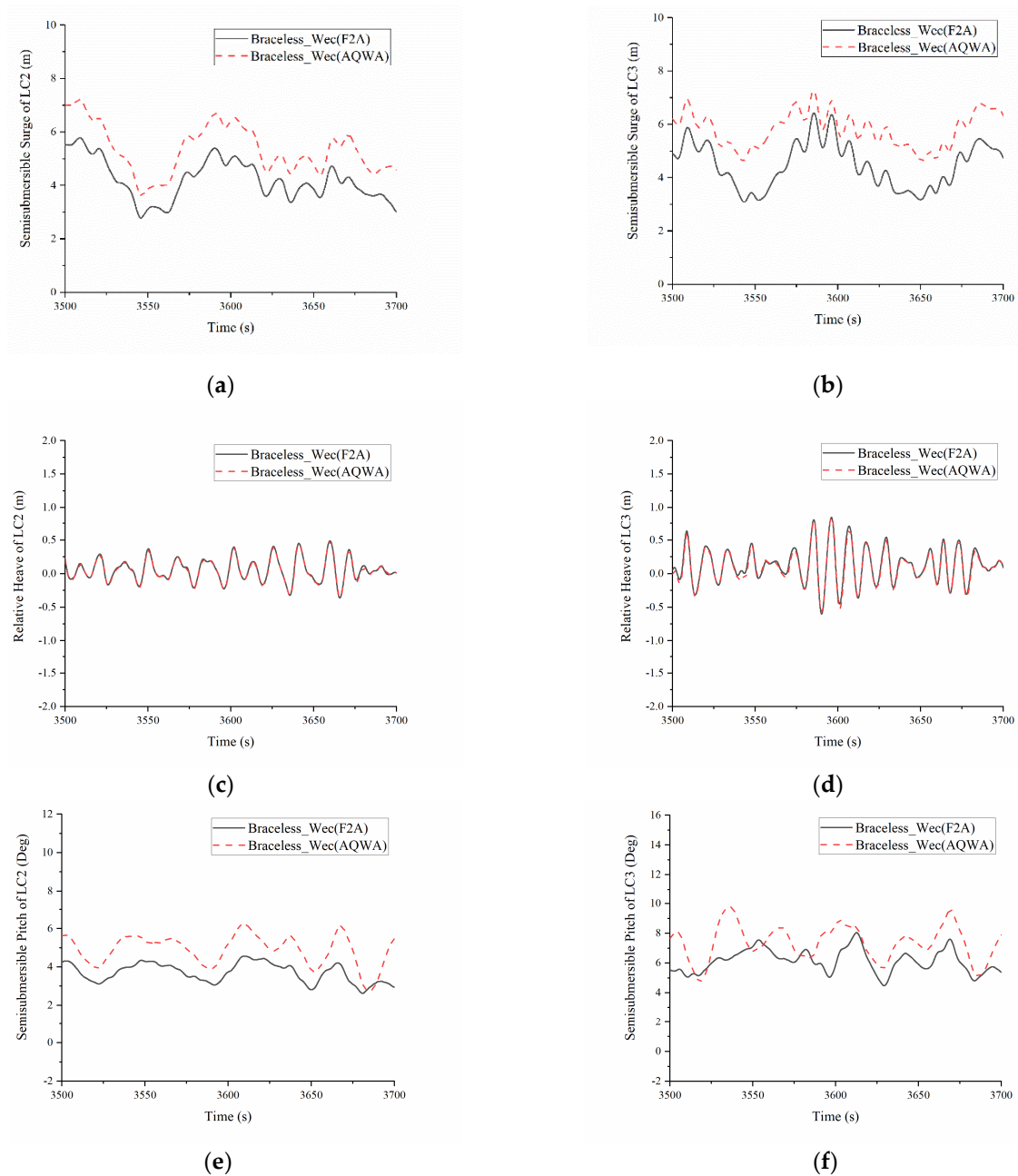
(**a**)

(**b**)

(**c**)

(**d**)

(**e**)

(**f**)

Figure 8. Time domain motion response of the semisubmersible platform: (**a**) Surge in LC2; (**b**) Surge in LC3; (**c**) Relative Heave in LC2; (**d**) Relative Heave in LC3; (**e**) Pitch in LC2; (**f**) Pitch in LC3.

Figure 9 shows motion response in LC4, in which the wind speed is larger than rated wind speed. Similar as the load case LC2 and LC3, the motion responses in surge and pitch direction from F2A are lower than those motions from AQWA due to the aerodynamic damping. The relative heave motions predicted from two codes are similar to each other.
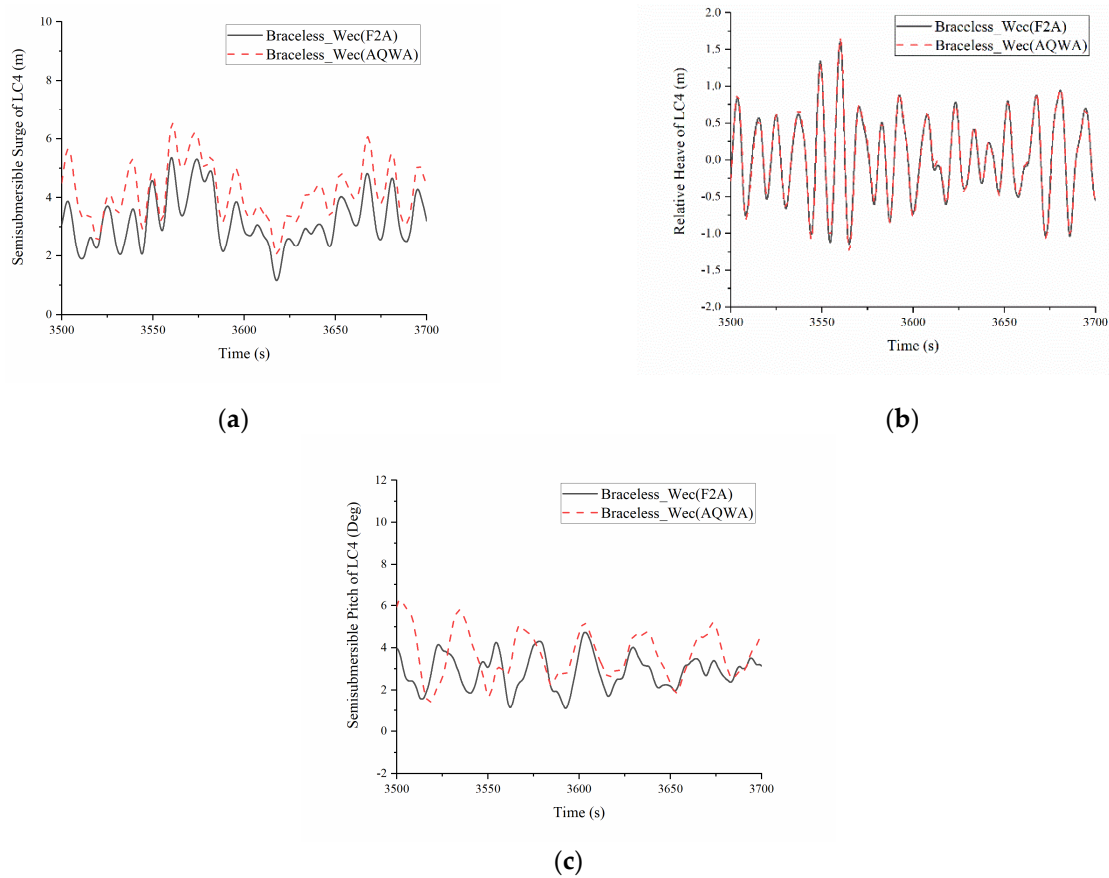
(a)

(b)

(c)

Figure 9. Motion responses of the semisubmersible platform in LC4: (**a**) Surge; (**b**) Relative Heave; (**c**) Pitch.

4.3.2. Mooring Line Force

The mooring line forces of ML1 and ML2 from LC2, LC3, and LC4 were compared for F2A results and AQWA in Figure 10. Basically, the mooring line force of ML2 in the upwind direction is larger than the mooring line force of ML1 in the downwind direction because wind and wave will drive the combined system to move in a downwind direction from its equilibrium position. Therefore, ML1 will get relaxed and ML2 will get tensioned. For the mooring line force of ML1, the reduction of the mooring force from its force at equilibrium position from F2A simulation is less than the reduction of the force from AQWA simulation due to the difference of the surge motions from two codes in all three load cases. Thus, the mooring line forces of ML1 from F2A are larger than those from AQWA (Figure 10a,c,e). However, for mooring line force of ML2, the increasing of the mooring force from its force at equilibrium position from F2A simulation is less than the increasing of force from AQWA simulation. Therefore, the mooring line forces of ML2 from F2A are less than those from AQWA (Figure 10b,d,f). Due to the pitch control above the rated wind speed (LC4), the wind thrust force is much smaller than that in LC2 (below rated wind speed) and LC3 (at rated wind speed). Therefore, the aerodynamic damping effect is much smaller. In this case (LC4), the contribution from wave load is much larger than wind load, and the discrepancy from two codes is minimal. Therefore, there is a slight difference in the mooring line force of ML2 for LC4.
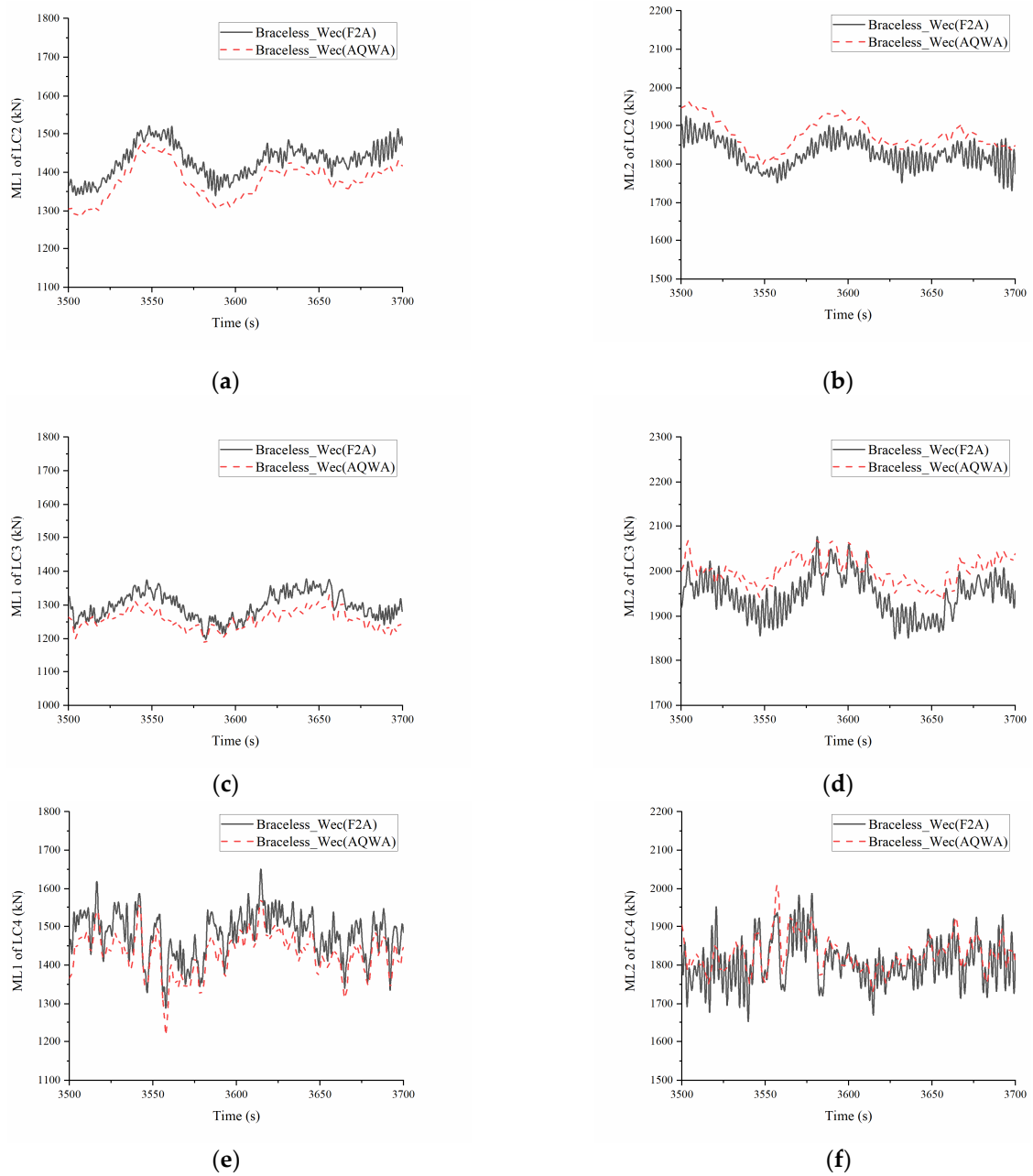
Figure 10. Mooring force of: (**a**) ML1 in LC2, (**b**) ML2 in LC2, (**c**) ML1 in LC3, (**d**) ML2 in LC3, (**e**) ML1 in LC4, (**f**) ML2 in LC4.

4.3.3. Produced Wave Power

The relative heave velocities between the semisubmersible platform and the WEC, the damping force and produced power from WEC in LC2, LC3, and LC4, are presented in Figure 11. Due to less effect of aerodynamic damping on heave motion, no significant difference is identified for the relative heave velocities, damping force, and produced power. When the wave height increases from LC2 to LC4, the relative heave velocity (Figure 11a,c,e) also increases due to the large relative heave motion in a severe sea state, which is beneficial to capture wave energy. Figure 11b,d,f present the vertical damping force. The F2A and AQWA simulation results were similar. As the wave height increases, the vertical damping force increases significantly. Figure 11g,h,i show the produced energy power from WEC. With the sea state moving from mild to severe (LC2 to LC4), more power can be produced from the wave. Figure 11i is the produced power under severe sea conditions (LC4). It can be seen the maximum power in LC4 is even as large as 3.5 MW (not shown in Figure 11f), which is comparable to the power produced from the wind turbine.

However, the mean produced power is less than 600 kW, and it shows obvious instability, while the produced power of WEC is much smaller. Therefore, the wind power production for NREL 5 MW WT will make the main contribution to the total power production of the combined system under the severe sea conditions.
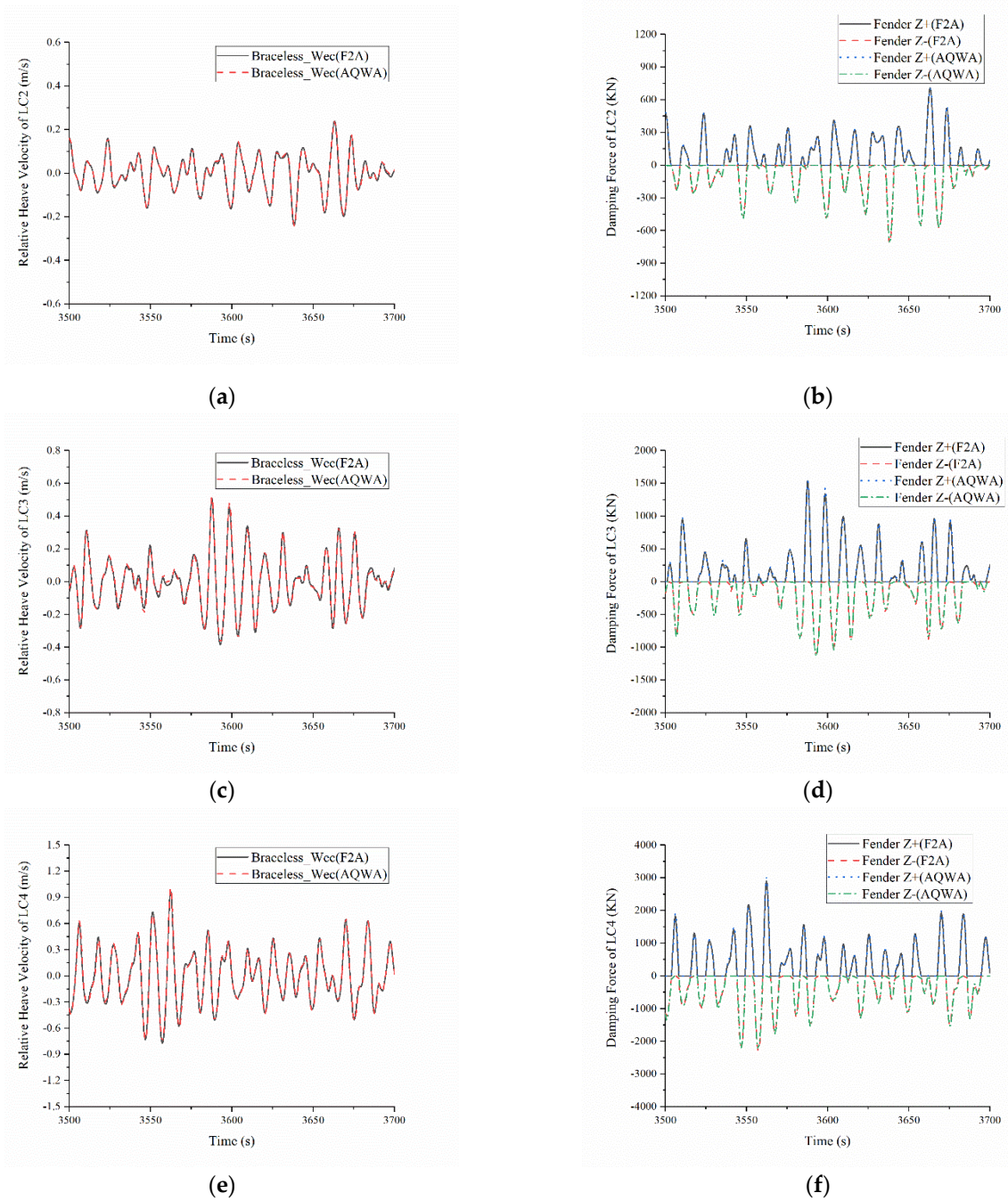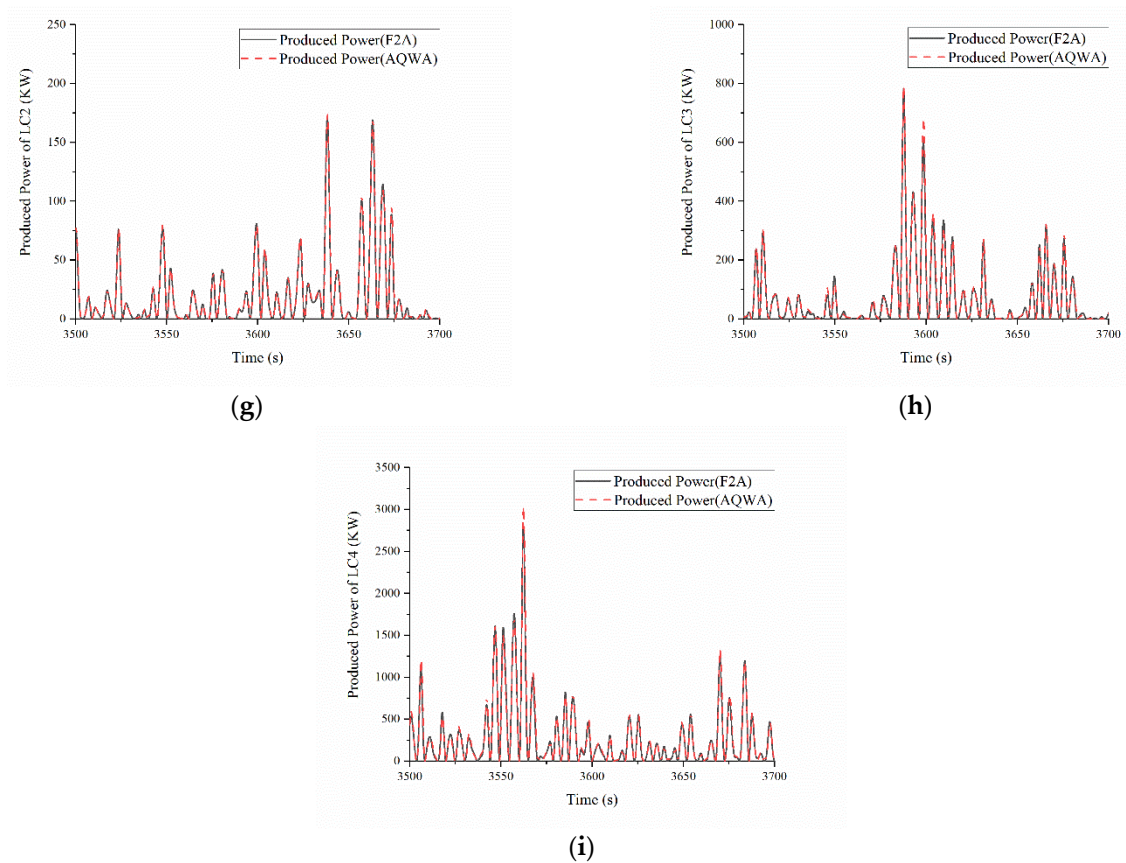

(a)

(b)

(c)

(d)

(e)

(f)

Figure 11. *Cont.*

(g)

(h)

(i)

Figure 11. Time series of different responses of the combined structure: (**a**) Relative Heave Velocity of LC2, (**b**) Damping Force of LC2, (**c**) Relative Heave Velocity of LC3, (**d**) Damping Force of LC3, (**e**) Relative Heave Velocity of LC4, (**f**) Damping Force of LC4, (**g**) Produced Power of LC2, (**h**) Produced Power of LC3, (**i**) Produced Power of LC4.

4.3.4. Statistical Analysis

Figure 12 displays the statistics of responses in operational conditions from both F2A simulation and AQWA simulation. The maximum and minimum values are determined as the highest crest and lowest trough of the corresponding time series. Figure 12a–c show that the simulation results of F2A and AQWA were different in the surge and pitch motion, and the heave motion results were slightly different, which was consistent with the previous results. When the wind velocity was the rated wind velocity of the wind turbine (12.4 m/s), the surge and pitch motion amplitudes of the platform were the largest, and the heave motion was greatly affected by the hydrodynamic load. When the wave height increases (LC2–LC4), the heave amplitude increases accordingly. Figure 12d shows that under the three operational conditions, the statistical values of the mooring force of ML2 simulated by F2A and AQWA were slightly different. Similarly, when the wind velocity was the rated wind velocity of 12.4 m/s (LC3), the mooring force of ML2 was the largest. Figure 12e shows that as the sea state becomes worse (LC2–LC4), the damping force and the produced power increase sharply. By comparing, aerodynamic loads were confirmed to have significant effects on surge and pitch motion and mooring forces, while hydrodynamic loads had significant effects on the vertical responses (heave, damping force, and produced power).
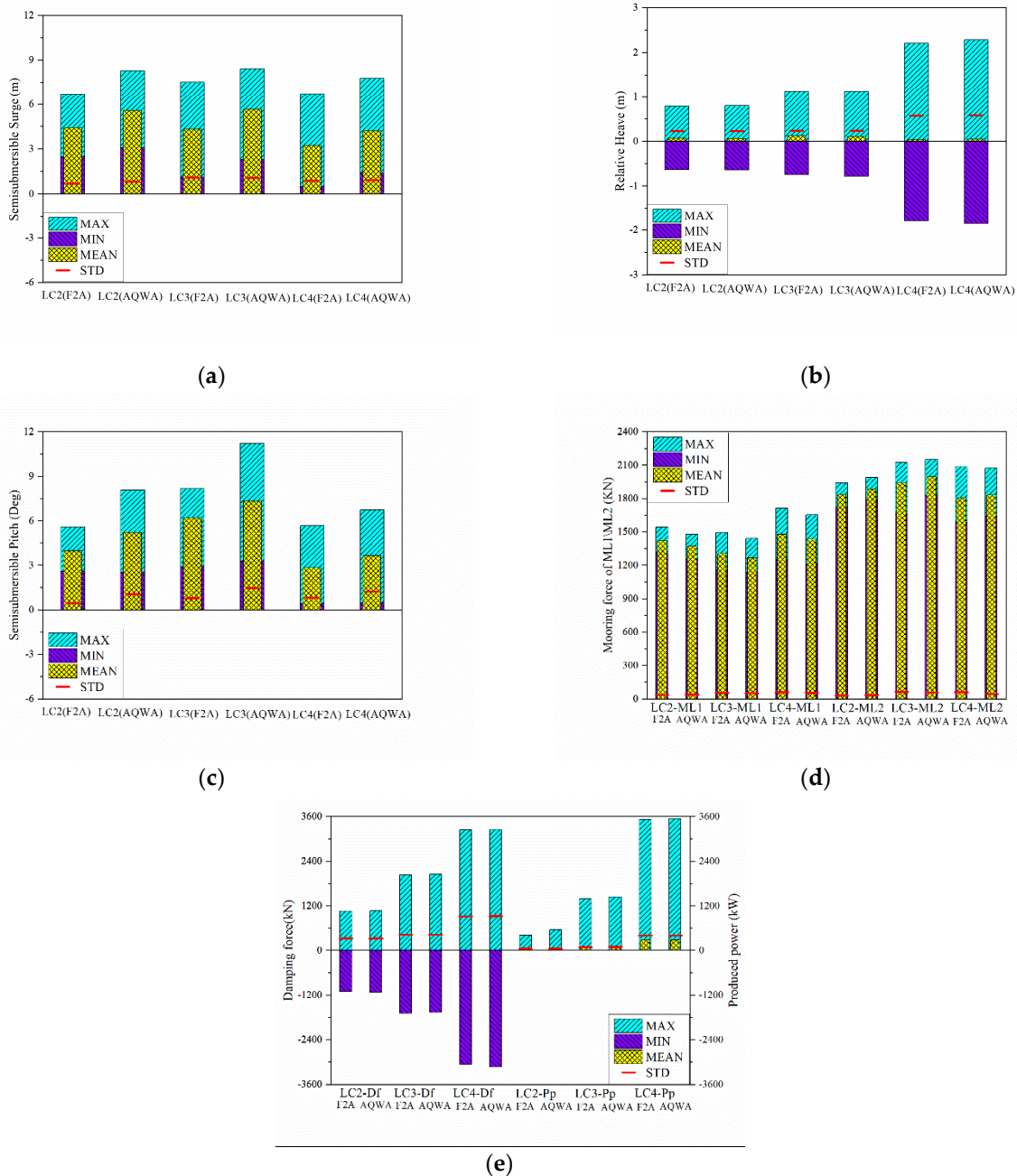
Figure 12. Comparison of the statistical results of in LC2, LC3, LC4: (**a**) Surge Motion; (**b**) Relative Heave Motion; (**c**) Pitch Motion; (**d**) Mooring Force of ML1 and ML2; (**e**) Damping Force (Df) and Produced Power (Pp).

4.4. Spectrum Analysis

In this section, the power spectral density (PSD) of platform motion response, mooring line force, damping force, and produced wave power were presented and compared for F2A simulation and AQWA simulation.

4.4.1. Motion Spectrum

Figure 13a,d,g display the PSD of the platform surge under the three load cases. The energy was mainly concentrated in the natural frequency of the surge and the wave frequency. For the mild sea state (LC2) in Figure 13a, there is a reduction for surge motion at the surge resonance peak in F2A simulation compared with AQWA simulation due to the aerodynamic damping effect. However, this reduction is not significant for worse sea state (LC3 and LC4) for surge motion in Figure 13d,g. For the relative heave motion, the

responses are dominated by the frequency from 0.3 to 0.9 rad/s which is related to the wave peak frequency. Therefore, both F2A simulation and AQWA simulation are very similar to each other (Figure 13b,e,h). Figure 13c,f,i are the PSD of the platform pitch motion. Observing the PSD curves of surge and pitch, the reason for the difference in the low frequency area around pitch resonance peak was the influence of aerodynamic damping considered in F2A simulation. It was obvious that when the wind velocity was small, aerodynamic damping obviously reduced the resonance response in the low-frequency region but had little effect on the wave frequency range. This phenomenon conforms well to the known characteristics of the general damping effect. However, when the wind velocity gradually increased (LC2–LC4), the influence of air damping gradually decreased. This was because the aerodynamic thrust acting on the rotor increases rapidly with increasing wind velocity, offsetting the increase in the aerodynamic damping effect caused by surge. Among these effects, aerodynamic damping and wind velocity had a first-order relationship, and aerodynamic thrust and wind velocity had a quadratic relationship. Therefore, at low wind velocities, aerodynamic damping had a greater influence, and at high wind velocities, aerodynamic thrust had a more obvious influence. It can be found that aerodynamic damping had a greater impact on pitch than surge and a stronger reduction in pitch motion.
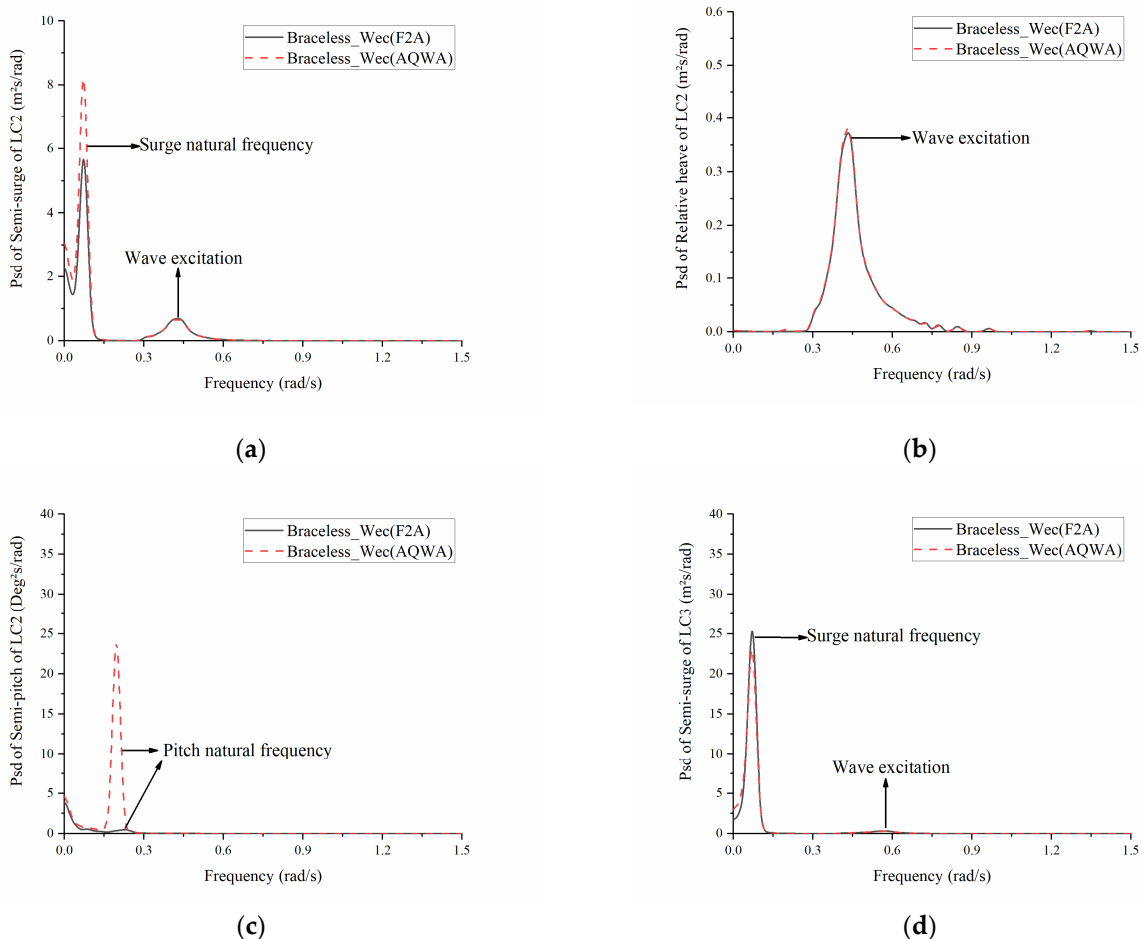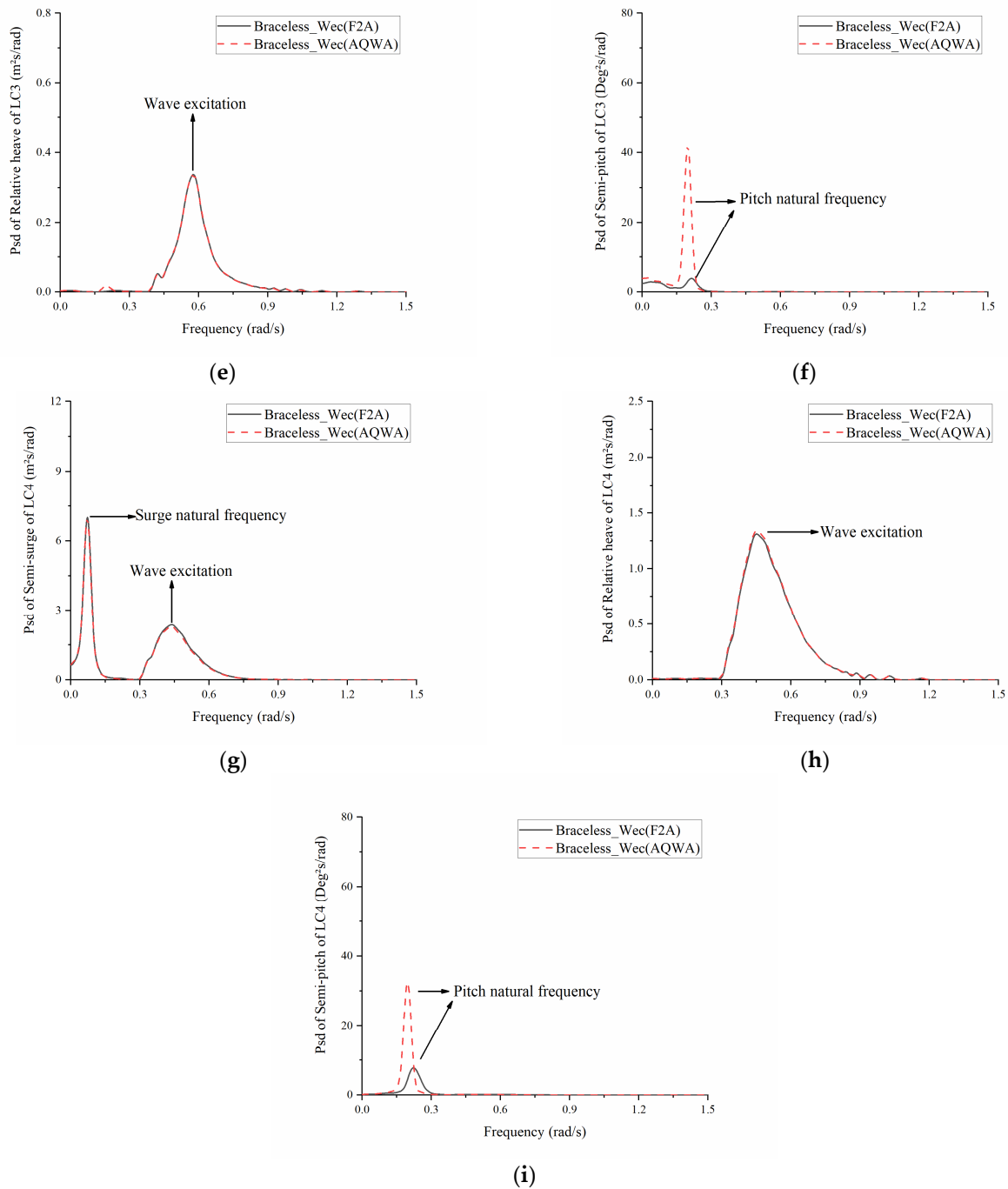

(a)

(b)

(c)

(d)

Figure 13. *Cont.*

Figure 13. Comparisons of the PSD of the motion for LC2, LC3, and LC4: (**a**) Surge Motion of LC2; (**b**) Relative Heave Motion of LC2; (**c**) Pitch Motion of LC2; (**d**) Surge Motion of LC3; (**e**) Relative Heave Motion of LC3; (**f**) Pitch of LC3; (**g**) Surge Motion of LC4; (**h**) Relative Heave Motion of LC4; (**i**) Pitch Motion of LC4.

4.4.2. Mooring Tension Spectrum

The mooring line responses in the frequency domain in the head sea under different load cases from F2A simulation and AQWA simulation are shown in Figure 14. For all the load cases, the most significant contribution to the ML 1 and ML2 tension comes from the low-frequency region (surge mode response). The contributions from pitch mode response are also identified. For worse sea state (LC4), the contributions to the ML1 and ML2 tension from the wave frequency range from 0.3 rad/s to 0.9 rad/s are comparable to the contribution from surge mode response. Similar to the PSD of the motion response, in the F2A simulation, aerodynamic damping had a weakening effect on the response

at surge and pitch natural frequencies. With the wind velocity increases (LC2–LC4), the aerodynamic damping effect gradually decreased.
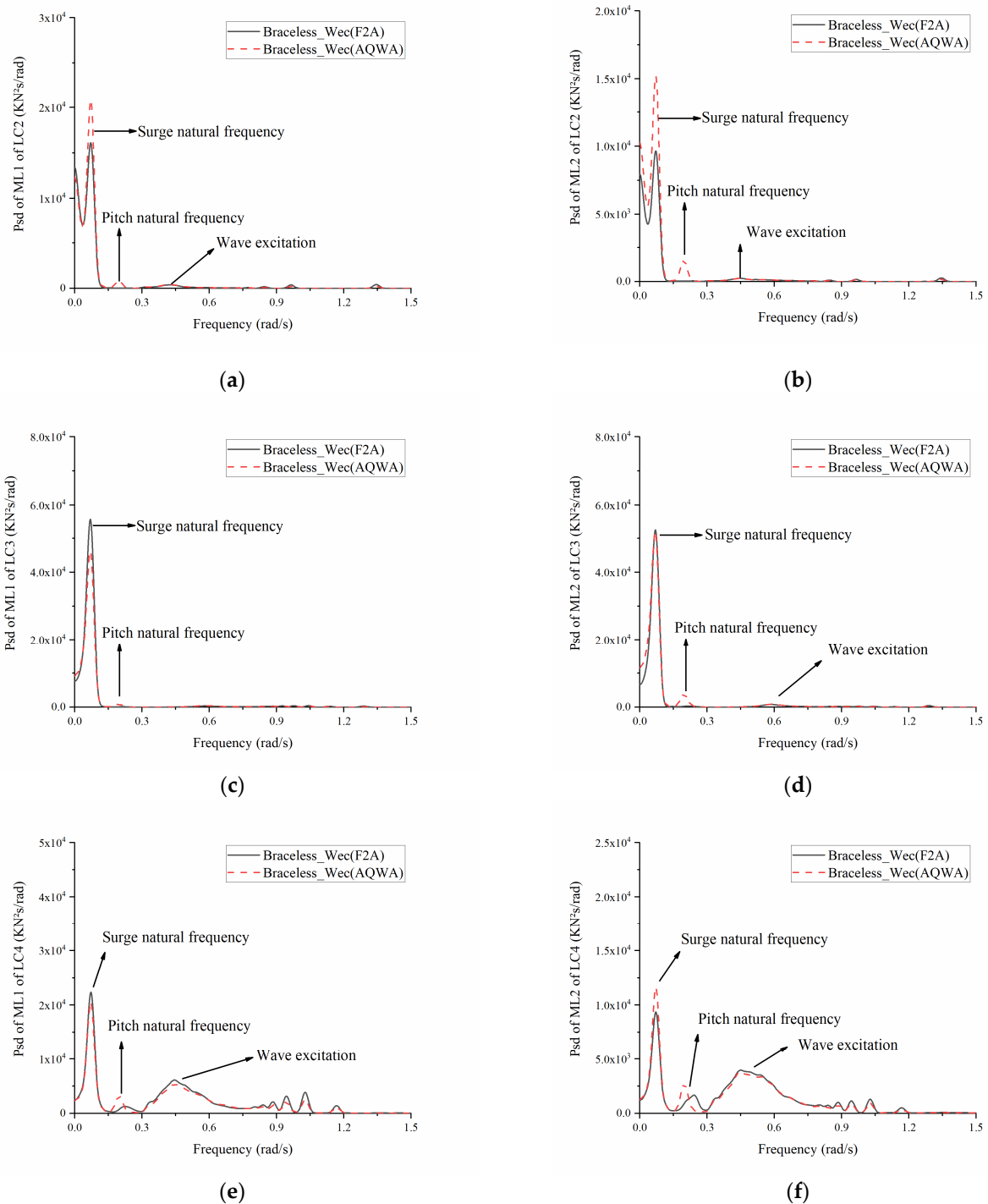

Figure 14. Comparisons of the PSD of the mooring line force of: (**a**) ML1 of LC2; (**b**) ML2 of LC2; (**c**) ML1 of LC3; (**d**) ML2 of LC3; (**e**) ML1 of LC4; (**f**) ML2 of LC4.

4.4.3. Damping Force and Produced Wave Power Spectrum

Figure 15 shows the damping force in the vertical direction and the produced wave energy power. The simulation results of the two simulation tools are slightly different. The energy was mainly concentrated in the wave frequency. Figure 15b,d,f are the PSDs of the produced power. The produced wave power frequencies are located in the dou-

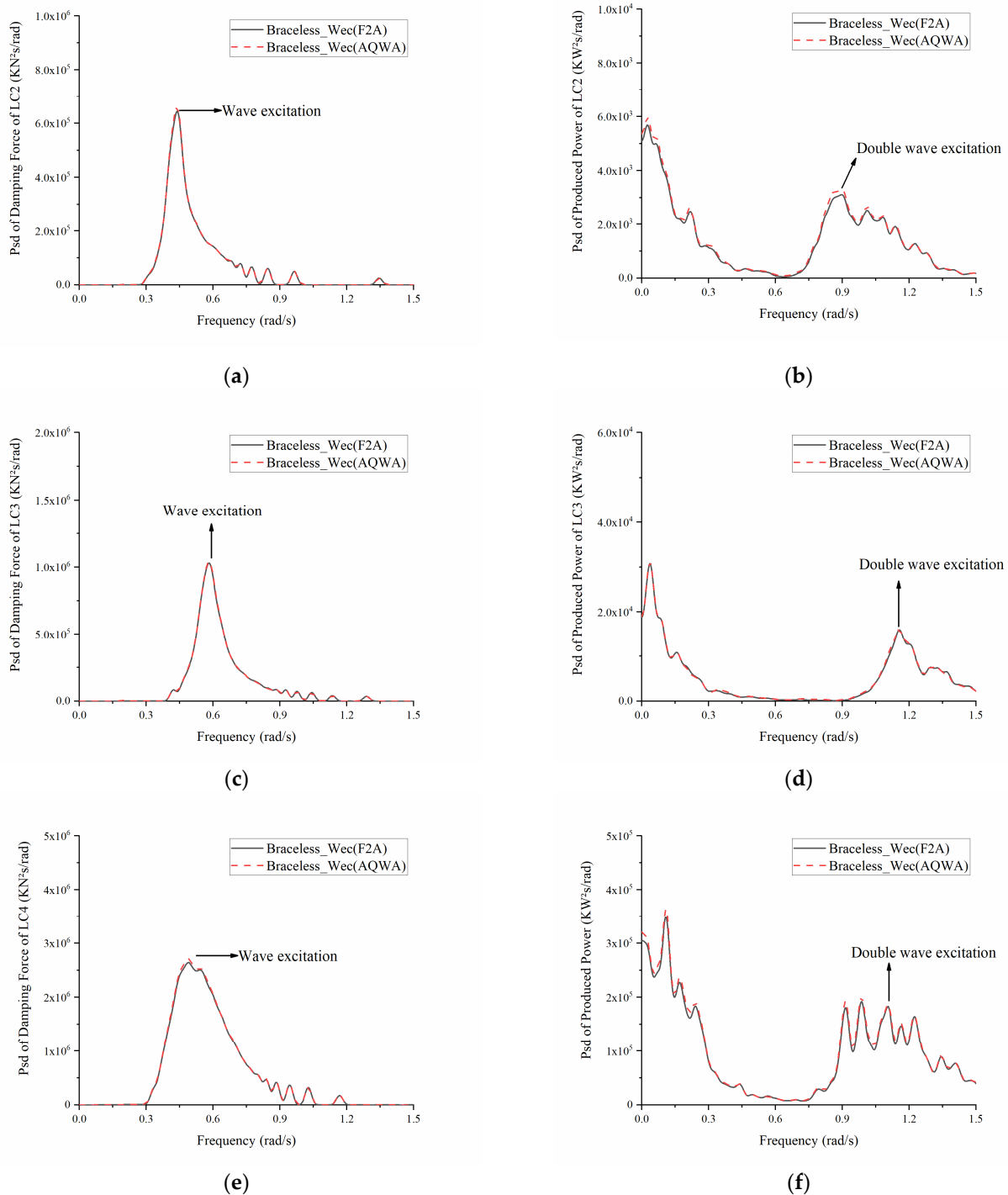ble wave frequency and low frequency regions. There was no significant effect from aerodynamic damping.

(a)

(b)

(c)

(d)

(e)

(f)

Figure 15. Comparisons of the PSD of: (**a**) Damping Force of LC2; (**b**) Produced Power of LC2; (**c**) Damping Force of LC3; (**d**) Produced Power of LC3; (**e**) Damping Force of LC4; (**f**) Produced Power of LC4.

4.5. Dynamic Responses in Extreme Conditions

Under extreme condition (LC5), the WEC and the semisubmersible platform were locked to each other, and there was no relative motion. The PTO system and the wind turbine were parked. As shown in Figure 16a, the WEC and the semisubmersible platform had the same heave motion and were in a locked state. Figure 16b,c show the PSDs of the

platform surge and heave. The PSD of the platform surge was mainly dominated by the wave frequency and the natural frequency of the surge. The PSD of the platform heave was mainly dominated by the wave frequency. From the PSD of the pitch (Figure 16e), it can be seen that the energy was mainly concentrated on the wave frequency and the natural frequency of the pitch, but the resonance effect on the pitch simulated by AQWA was much smaller than the result of the F2A simulation. When using F2A simulation, the upper wind turbine was parked, and the pitch angle was set to 90°. Figure 16e,f show the mooring forces of ML1 and ML2. The energy was mainly dominated in the wave frequency range.
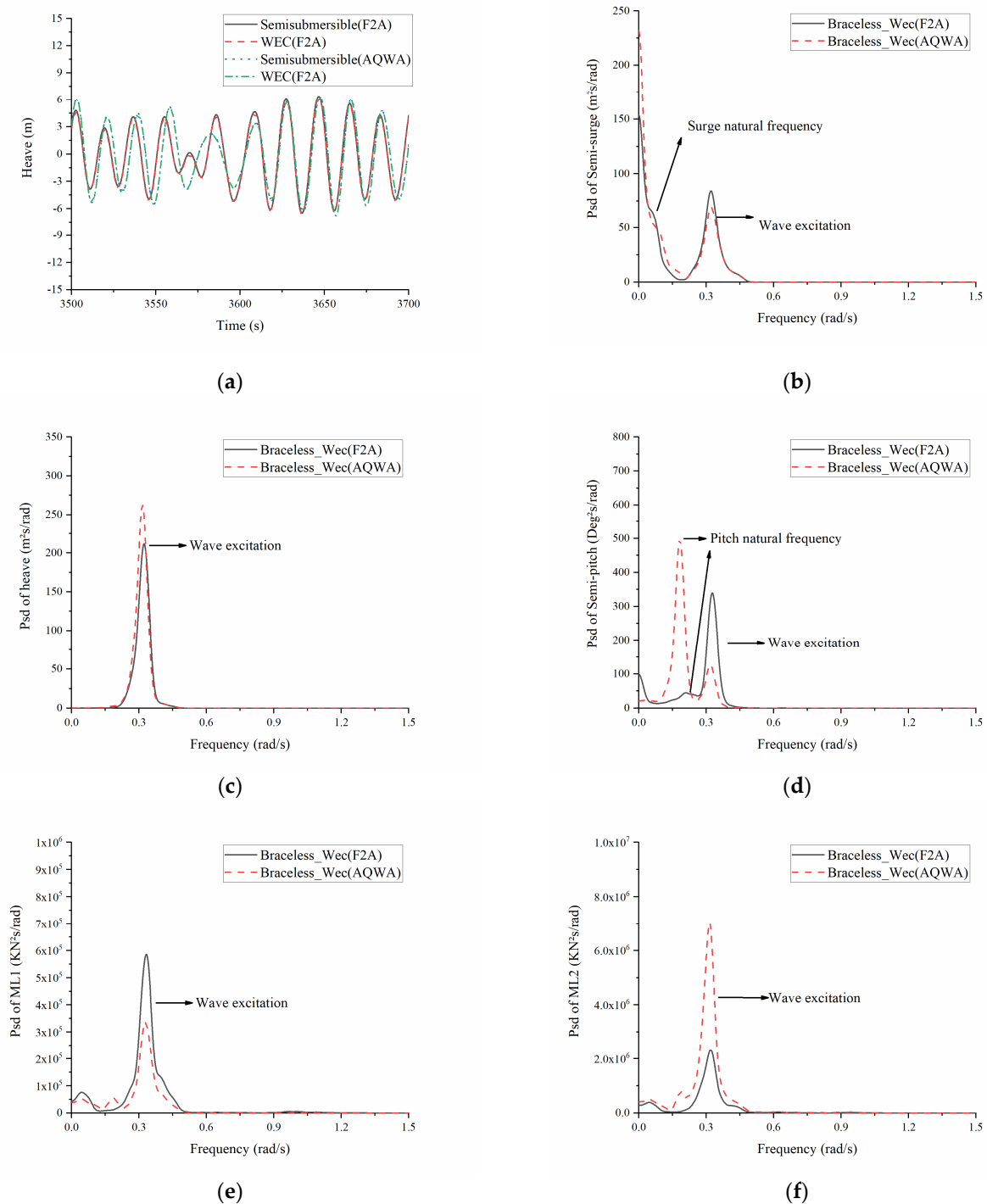

Figure 16. Motion and mooring force response of the platform under LC5: (**a**) Heave motion time series; (**b**) PSD of platform surge; (**c**) PSD of platform heave; (**d**) PSD of platform pitch; (**e**) PSD of ML1; (**f**) PSD of ML2.

5. Conclusions

In this study, through a recently proposed fully coupled analysis framework (F2A), a fully coupled analysis of a combined system consisting of a semisubmersible platform (braceless) and a heaving-type WEC was carried out. A numerical model of the combined structure that was capable of simulating its motion and dynamic responses under different typical operational and extreme conditions was developed and used. Different types of analysis and comparison were performed to examine the fully coupled responses of the combined structure. The primary results are summarized as follows:

(1) Under regular wave conditions, regardless of wind conditions, the simulation results of F2A and AQWA were basically similar in time domain motion, mooring force, and generated wave power. Since F2A integrated the AQWA hydrodynamic module, it shows that F2A has good consistency with AQWA.

(2) Under irregular wave and turbulent wind conditions, F2A and AQWA had significant differences in time domain motion and mooring force. It shows that F2A effectively reduces the dynamic response amplitude because of the aerodynamic damping effect in F2A; as the wave and wind velocity increased, the amplitude of time-domain motion and mooring force (ML2) are significantly affected by aerodynamic loads, and the dynamic response amplitudes are the largest at rated wind velocity. The trends of relative heave motion, damping force, and produced wave power were similar.

(3) Through the PSD analysis of the dynamic response, it was more obvious that aerodynamic damping used F2A effectively inhibited the resonance at the low frequency range, which was the largest difference compared to the prediction calculated with the simulation tool of AQWA. The relationship between aerodynamic damping and wind velocity was linear, and the relationship between aerodynamic thrust and wind velocity was quadratic. Therefore, when the wind velocity was small, the influence of aerodynamic damping was significant, and especially the resonance of surge and pitch was significantly reduced. When the wind velocity increased, the aerodynamic thrust had a significant effect. The inhibition effect of aerodynamic damping was mainly concentrated in the low-frequency region and had no obvious effect on the resonance caused by the wave frequency. The resonance was mainly excited near the wave frequency; there was a slight difference between F2A and AQWA simulation results close to resonance.

(4) Under extreme conditions, the WEC was locked on a semisubmersible platform as a way of survival to withstand the impact of large wave force. From the PSD analysis of time domain motion and mooring force, the energy was mainly concentrated near the wave frequency, and the wave influence was obvious.

References

1. World Wind Energy Association. Available online: https://wwindea.org/worldwide-wind-capacity-reaches-744-gigawatts (accessed on 24 March 2021).
2. Jonkman, J.; Butterfield, S.; Musial, W.; Scott, G. *Definition of a 5-MW Reference Wind Turbine for Offshore System Development*; National Renewable Energy Laboratory (NREL): Golden, CO, USA, 2009.
3. Bak, C.; Zahle, F.; Bitsche, R.; Kim, T.; Yde, A.; Henriksen, L.C.; Hansen, M.H.; Blasques, J.P.A.A.; Gaunaa, M.; Natarajan, A. *The DTU 10-MW Reference Wind Turbine*; Danish Wind Power Research: Lyngby, Denmark, 2013.
4. Roddier, D.; Cermelli, C.; Aubault, A.; Weinstein, A. WindFloat: A floating foundation for offshore wind turbines. *J. Renew. Sustain. Energy* **2010**, *2*, 033104. [CrossRef]
5. Huijs, F.; de Bruijn, R.; Savenije, F. Concept design verification of a semi-submersible floating wind turbine using coupled simulations. *Energy Procedia* **2014**, *53*, 2–12. [CrossRef]
6. Lefranc, M.; Torud, A. Three wind turbines on one floating unit, feasibility, design and cost. In Proceedings of the Offshore Technology Conference, Houston, TX, USA, 2–5 May 2011.
7. Le Boulluec, M.; Ohana, J.; Martin, A.; Houmard, A. Tank testing of a new concept of floating offshore wind turbine. In Proceedings of the ASME 2013 32nd International Conference on Ocean, Offshore and Arctic Engineering, Nantes, France, 9–14 June 2013.
8. Luan, C.; Gao, Z.; Moan, T. Design and analysis of a braceless steel 5-MW semi-submersible wind turbine. In Proceedings of the ASME 2016 35st International Conference on Ocean, Offshore and Arctic Engineering, Busan, Korea, 19–24 June 2016.
9. Karimirad, M.; Michailides, C. V-shaped semisubmersible offshore wind turbine: An alternative concept for offshore wind technology. *Renew. Energy* **2015**, *83*, 126–143. [CrossRef]
10. Robertson, A.; Jonkman, J.; Masciola, M.; Song, H.; Goupee, A.; Coulling, A.; Luan, C. *Definition of the Semisubmersible Floating System for Phase II of OC4*; National Renewable Energy Laboratory (NREL): Golden, CO, USA, 2014.
11. Falcão, A.F.D.O. Wave energy utilization: A review of the technologies. *Renew. Sustain. Energy Rev.* **2010**, *14*, 899–918. [CrossRef]
12. Aboutalebi, P.M.; Zoughi, F.; Garrido, I.; Garrido, A.J. Performance analysis on the use of oscillating water column in barge-based floating offshore wind turbines. *Mathematics* **2021**, *9*, 475. [CrossRef]
13. Aboutalebi, P.M.; Zoughi, F.; Martija, I.; Garrido, I.; Garrido, A.J. Switching control strategy for oscillating water columns based on response amplitude operators for floating offshore wind turbines stabilization. *Appl. Sci.* **2021**, *11*, 5249. [CrossRef]
14. Michailides, C.; Gao, Z.; Moan, T. Response analysis of the combined wind/wave energy concept sfc in harsh environmental conditions. In Proceedings of the RENEW2014 1st International Conference on Renewable Energies Offshore, Lisbon, Portugal, 24–26 November 2014.
15. Ren, N.; Ma, Z.; Shan, B.; Ning, D.; Ou, J. Experimental and numerical study of dynamic responses of a new combined TLP type floating wind turbine and a wave energy converter under operational conditions. *Renew. Energy* **2020**, *151*, 966–974. [CrossRef]
16. Bachynski, E.E.; Moan, T. Point absorber design for a combined wind and wave energy converter on a tension-leg support structure. In Proceedings of the ASME 32nd International Conference on Ocean, Offshore and Arctic Engineering, Nantes, France, 9–14 June 2013.
17. Russo, S.; Contestabile, P.; Bardazzi, A.; Leone, E.; Iglesias, G.; Tomasicchio, G.R.; Vicinanza, D. Dynamic loads and response of a spar buoy wind turbine with pitch-controlled rotating blades: An experimental study. *Energies* **2021**, *14*, 3598. [CrossRef]
18. Tomasicchio, G.R.; Vicinanza, D.; Belloli, M.; Lugli, C.; Latham, J.P.; Iglesias Rodriguez, J.G.; Jensen, B.; Vire, A.; Monbaliu, J.; Taruffi, F.; et al. Physical model tests on spar buoy for offshore floating wind energy conversion. *Ital. J. Eng. Geol. Environ.* **2020**, *1*, 129–143.
19. Xu, X.; Day, S. Experimental investigation on dynamic responses of a spar-type offshore floating wind turbine and its mooring system behaviour. *Ocean Eng.* **2021**, *236*, 109488. [CrossRef]
20. Hu, J.; Zhou, B.; Vogel, C.; Liu, P.; Willden, R.; Sun, K.; Zang, J.; Geng, J.; Jin, P.; Cui, L.; et al. Optimal design and performance analysis of a hybrid system combing a floating wind platform and wave energy converters. *Appl. Energy* **2020**, *269*, 114998. [CrossRef]
21. Sarmiento, J.; Iturrioz, A.; Ayllón, V.; Guanche, R.; Losada, I.J. Experimental modelling of a multi-use floating platform for wave and wind energy harvesting. *Ocean Eng.* **2019**, *173*, 761–773. [CrossRef]
22. Marina Platform. Available online: https://www.msp-platform.eu/projects/marina-platform (accessed on 3 April 2020).
23. Peiffer, A.; Roddier, D.; Aubault, A. Design of a point absorber inside the WindFloat structure. In Proceedings of the ASME 2011 30th International Conference on Ocean, Offshore and Arctic Engineering, Rotterdam, The Netherlands, 19–24 June 2011.
24. Aubault, A.; Alves, M.; Sarmento, A.N.; Roddier, D.; Peiffer, A. Modeling of an oscillating water column on the floating foundation WindFloat. In Proceedings of the ASME 2011 30th International Conference on Ocean, Offshore and Arctic Engineering, Rotterdam, The Netherlands, 19–24 June 2011.
25. Muliawan, M.J.; Karimirad, M.; Moan, T. Dynamic response and power performance of a combined Spar-type floating wind turbine and coaxial floating wave energy converter. *Renew. Energy* **2013**, *50*, 47–57. [CrossRef]
26. Muliawan, M.J.; Karimirad, M.; Gao, Z.; Moan, T. Extreme responses of a combined spar-type floating wind turbine and floating wave energy converter (STC) system with survival modes. *Ocean Eng.* **2013**, *65*, 71–82. [CrossRef]
27. Wan, L.; Gao, Z.; Moan, T. Experimental and numerical study of hydrodynamic responses of a combined wind and wave energy converter concept in survival modes. *Coast. Eng.* **2015**, *104*, 151–169. [CrossRef]

28. Wan, L.; Gao, Z.; Moan, T.; Lugni, C. Experimental and numerical comparisons of a combined wind and wave energy converter concept under operational conditions. *Renew. Energy* **2016**, *93*, 87–100. [CrossRef]
29. Wan, L.; Gao, Z.; Moan, T.; Lugni, C. Comparative experimental study of the survivability of a combined wind and wave energy converter in two testing facilities. *Ocean Eng.* **2016**, *111*, 82–94. [CrossRef]
30. Michailides, C.; Gao, Z.; Moan, T. Experimental study of the functionality of a semisubmersible wind turbine combined with flap-type Wave Energy Converters. *Renew. Energy* **2016**, *93*, 675–690. [CrossRef]
31. Michailides, C.; Gao, Z.; Moan, T. Experimental and numerical study of the response of the offshore combined wind/wave energy concept SFC in extreme environmental conditions. *Mar. Struct.* **2016**, *50*, 35–54. [CrossRef]
32. Michailides, C.; Luan, C.; Gao, Z.; Moan, T. Effect of flap type wave energy converters on the response of a semi-submersible wind turbine in operational conditions. In Proceedings of the ASME 2014 33rd International Conference on Ocean, Offshore and Arctic Engineering, San Francisco, CA, USA, 8–13 June 2014.
33. Ren, N.; Ma, Z.; Fan, T.; Zhai, G.; Ou, J. Experimental and numerical study of hydrodynamic responses of a new combined monopile wind turbine and a heave-type wave energy converter under typical operational conditions. *Ocean Eng.* **2018**, *159*, 1–8. [CrossRef]
34. Wang, Y.; Zhang, L.; Michailides, C.; Wan, L.; Shi, W. Hydrodynamic response of a combined wind-wave marine energy structure. *J. Mar. Sci. Eng.* **2020**, *8*, 253. [CrossRef]
35. Le Cunff, C.; Heurtier, J.; Piriou, L.; Berhault, C.; Perdrizet, T.; Teixeira, D.; Ferrer, G.; Gilloteaux, J.C. Fully coupled floating wind turbine simulator based on nonlinear finite element method: Part I—Methodology. In Proceedings of the ASME 2013 32nd International Conference on Ocean, Offshore and Arctic Engineering, Nantes, France, 9–14 June 2013.
36. Perdrizet, T.; Gilloteaux, J.; Teixeira, D.; Ferrer, G.; Piriou, L.; Cadiou, D.; Heurtier, J.M.; Le Cunff, C. Fully coupled floating wind turbine simulator based on nonlinear finite element method: Part II—Validation Results. In Proceedings of the ASME 2013 32nd International Conference on Ocean, Offshore and Arctic Engineering, Nantes, France, 9–14 June 2013.
37. Chen, J.; Hu, Z.; Liu, G.; Wan, D. Coupled aero-hydro-servo-elastic methods for floating wind turbines. *Renew. Energy* **2019**, *130*, 139–153. [CrossRef]
38. Jonkman, J.M. Dynamics of offshore floating wind turbines-model development and verification. *Wind Energy* **2009**, *12*, 459–492. [CrossRef]
39. Jonkman, J.M. *Dynamics Modeling and Loads Analysis of an Offshore Floating Wind Turbine*; National Renewable Energy Laboratory (NREL): Golden, CO, USA, 2007.
40. Kvittem, M.I.; Bachynski, E.E.; Moan, T. Effects of hydrodynamic modelling in fully coupled simulations of a semi-submersible wind turbine. *Energy Procedia* **2012**, *24*, 351–362. [CrossRef]
41. Shim, S. Coupled Dynamic Analysis of Floating Offshore Wind Farms. Ph.D. Thesis, Texas A & M University, College Station, TX, USA, 2010.
42. Yang, Y.; Bashir, M.; Michailides, C.; Li, C.; Wang, J. Development and application of an aero-hydro-servo-elastic coupling framework for analysis of floating offshore wind turbines. *Renew. Energy* **2020**, *161*, 606–625. [CrossRef]
43. *AQWA Manual Release 19.0*; ANSYS Inc.: Canonsburg, PA, USA, 2018.
44. Moriarty, P.J.; Hansen, A.C. *AeroDyn Theory Manual*; National Renewable Energy Laboratory (NREL): Golden, CO, USA, 2005.
45. Chen, J.; Hu, Z. Experimental investigation of aerodynamic effect-induced dynamic characteristics of an OC4 semi-submersible floating wind turbine. *Proc. Inst. Mech. Eng. Part M J. Eng. Marit. Environ.* **2018**, *231*, 19–36. [CrossRef]
46. Karimirad, M.; Moan, T. Effect of aerodynamic and hydrodynamic damping on dynamic response of a spar type floating wind turbine. *Development* **2010**, *2*, 3.
47. Faltinsen, O. *Sea Loads on Ships and Offshore Structures*; Cambridge University Press: Cambridge, UK, 1993.
48. Li, Y.C.; Teng, B. *The Effect of Waves on Marine Buildings*, 3rd ed.; Ocean Publication: Beijing, China, 2015; pp. 270–273.
49. Morison, J.R.; Johnson, J.W.; Schaaf, S.A. The force exerted by surface waves on piles. *Pet. Trans. Aime* **1950**, *2*, 149–154. [CrossRef]
50. Wang, Y.; Shi, W.; Zhang, L.; Michailides, C.; Zhou, L. Hydrodynamic analysis of a floating hybrid renewable energy system. In Proceedings of the 30th International Society of Offshore and Polar Engineers, Shanghai, China, 14–19 June 2020.
51. Zhao, Y.; Yang, J.; He, Y.; Gu, M. Coupled dynamic response analysis of a multi-column tension-leg-type floating wind turbine. *China Ocean. Eng.* **2016**, *30*, 505–520. [CrossRef]